2018-07-01

Ion Friction at Small Values of the Coulomb Logarithm

Robert Tucker Sprenkle
Brigham Young University

Ion Friction at Small Values of the Coulomb Logarithm

Robert Tucker Sprenkle

A thesis submitted to the faculty of
Brigham Young University
in partial fulfillment of the requirements for the degree of

Master of Science

Scott Bergeson, Chair
Michael Ware
Ross Spencer

Department of Physics and Astronomy

Brigham Young University

ABSTRACT

Ion Friction at Small Values of the Coulomb Logarithm

Robert Tucker Sprenkle
Department of Physics and Astronomy, BYU
Master of Science

We create a dual-species ultracold neutral plasma (UNP) by photo-ionizing Yb and Ca atoms in a dual-species magneto-optical trap. Unlike single-species UNP expansion, these plasmas are well outside of the collisionless (Vlasov) approximation. We observe the mutual interaction of the Yb and Ca ions by measuring the velocity distribution for each ion species separately. We model the expansion using a fluid code including ion-ion friction and compare with experimental results to obtain a value of the Coulomb logarithm of $\Lambda = 0.04$.

ACKNOWLEDGMENTS

Tiffani Sprenkle: I cannot thank my wife, Tiffani, enough for all the sacrifices she has made in my behalf. I thank her for her time and endless support in helping me accomplish my dreams.

Dr. Bergeson: I am very grateful to Dr. Bergeson for his patience and willingness to teach me. I feel blessed for having such a great adviser who is knowledgeable in the field and active in the scientific community. I am grateful for all the one on one time we had in the lab and office where I could ask questions and fill/correct gaps in my understanding.

Committee: I thank my committee, Dr. Bergeson, Dr. Ware and Dr. Spencer for their time and support in guiding me in this work.

BYU: I am blessed for the opportunity to attend such a great university. I cherish my education and hope to stand as an example of the standards and quality of the university. I am grateful to Brigham Young University for providing the space and support for Dr. Bergeson's Lab where I performed this work.

Contents

List of Figures

Chapter 1

Introduction

Ultracold neutral plasmas open a unique window for studying strongly-coupled plasmas. High accuracy laser spectroscopy tools can be used in the ultracold low-energy system to diagnose the plasma state with extreme precision. Surprisingly, ultracold neutral plasmas share similarities with fusion-class plasmas. In both, the influence of nearest-neighbor collisions are more important than the influence of the much weaker, but much more frequent, long range collisions.

Of particular interest is the time scale for which the plasma returns to its equilibrium state, known as energy relaxation. In fusion systems, energetic alpha particles resulting from fusion need to deposit their energy back into the plasma to drive a self-sustaining reaction. Monte-Carlo simulations can be used to understand this energy relaxation process because direct measurements in fusion systems are somewhat challenging. In our experiment, we measure the energy relaxation in a Yb/Ca dual species ultracold neutral plasma where the mass ratio is nearly identical to the proton-to-alpha mass ratio. Thus, the study of ultracold neutral plasmas will give us information about fusion class plasmas [1].

Plasmas can be characterized using two dimensionless parameters. The first is the ratio of the nearest-neighbor electric potential energy to the average kinetic energy of the plasma. This is called

the strong coupling parameter Γ, given by

$$\Gamma = \frac{e^2}{4\pi\varepsilon_0 a_{ws}} \frac{1}{k_B T_i},$$ (1.1)

where $a_{ws} = (3/4\pi n)^{1/3}$ is the Wigner-Seitz radius, n is the density of the plasma, k_B is Boltzmann's constant and ε_0 is the vacuum permittivity constant, and T_i is the ion temperature of the plasma. For our experiment Γ is on the order of 2. The Coulomb logarithm in the Landau-Spitzer interpretation is given as the ratio of the Debye length, λ_D, to the classic distance of closest approach r_0,

$$\Lambda = \ln\frac{\lambda_D}{r_0},$$ (1.2)

although choices other than the Landau-Spitzer picture are made [34]. In this equation, $\lambda_D = \sqrt{\frac{\varepsilon_0 k_B T}{ne^2}}$ and $r_0 = \frac{e^2}{4\pi\varepsilon_0}\frac{1}{k_B T_i}$. Formally, the distance of closest approach, r_0, is the impact parameter corresponding to $90°$ deflection in the Rutherford scattering picture. We can rewrite the Coulomb logarithm in terms of the the strong coupling parameter, Γ, as

$$\Lambda = \ln\left[\left(3\Gamma^3\right)^{-1/2}\right].$$ (1.3)

We can see that large values of Λ means Γ must be small. This representation also puts a non-physical limit on $\Gamma = 3^{-1/3} = 0.693$. In the strongly coupled regime Γ is measured to be larger than 0.693 [35], making the Coulomb logarithm negative.

The second dimensionless parameter is the inverse scaled screening length, κ,

$$\kappa = \frac{a_{ws}}{\lambda_D}.$$ (1.4)

From this equation we find that $\kappa \propto n^{1/6}/T_e^{1/2}$. Larger values of κ correspond to stronger electron screening, effectively reducing the influence of nearest neighbor collisions. Both κ and Γ are used in characterizing strongly coupled plasmas. The red line in Fig. 1.1 shows the dividing line for strongly and weakly coupled plasmas, where $\Gamma = 1$

In a dual species Ca/Yb plasma the dimensionless plasma parameters are $\Gamma \approx 2$, $\kappa = 0.5$,
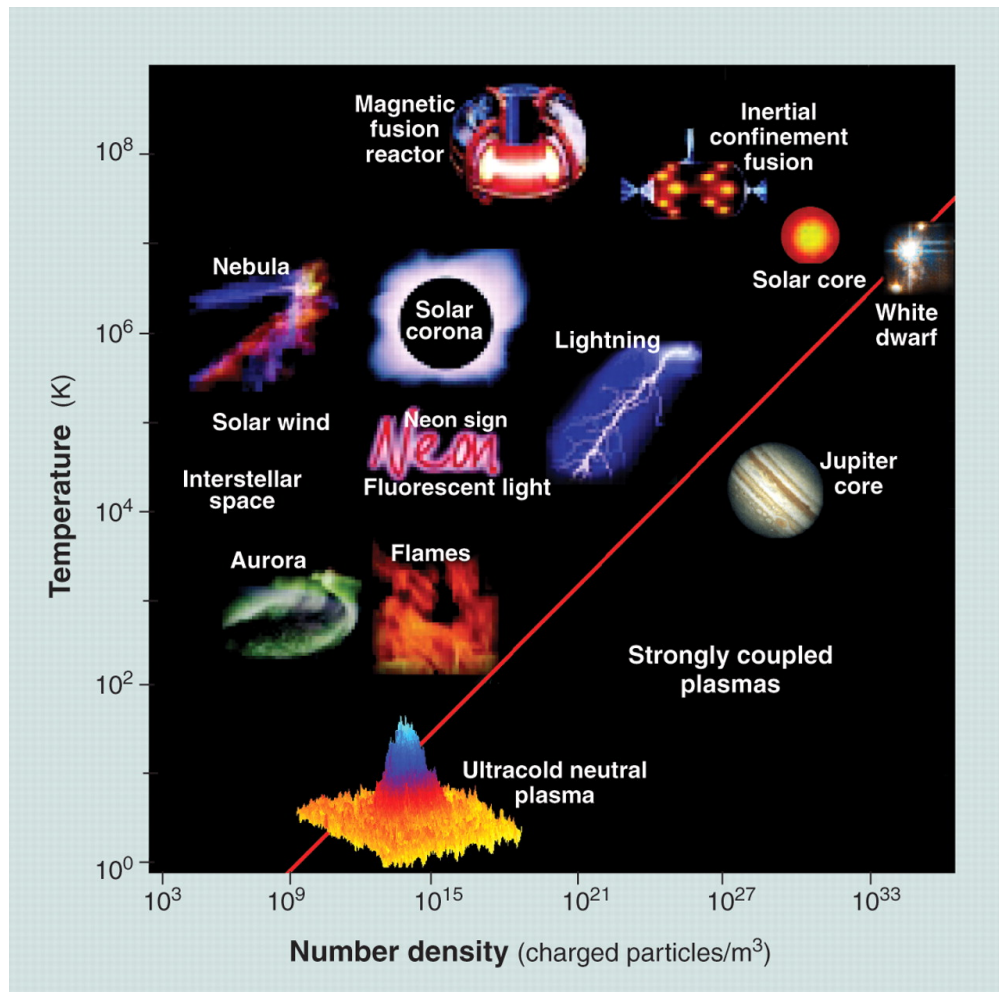
Figure 1.1 This figure shows the many different forms of plasmas. The red line indicates $\Gamma = 1$. Ultracold neutral plasmas exist in the high density low temperature regime where $\Gamma > 0$. [36]

and in the Landau-Spitzer picture $\Lambda < 0$. The standard plasma collisional cross-section for the ions in the plasma is proportional to Λ. A negative value is clearly nonphysical and indicates the failure of standard kinetic plasma models. Molecular dynamics (MD) simulations have become a valuable alternative to kinetic theory in trying to model such strongly coupled plasmas for finding better values for the Coulomb logarithm [3]. These MD models, while helpful, need experimental verification. Our aim is to provide an expression for the Coulomb logarithm in the strongly coupled regime that can be used to verify MD simulations.

Using the precision of laser spectroscopy we are able to measure the time-dependent velocity of ions in a strongly coupled plasma. We develop a particle in cell (PIC) method for modeling the dual species evolution and compare with experimental results. Comparing the model and the data provide values for the Coulomb logarithm that are used to verify the Coulomb logarithm that extends into the strongly coupled regime.

Previous studies of strongly coupled plasmas include measurements of three body recombination rates [4–10, 19–21], plasma wave damping [11–13], and DC and RF Plasma response [14–18]. Computational work also provides insights into energy relaxation expectations [3, 22–26]. All previous work in this field has used a single species plasma. Our work will be measuring the energy relaxation of a dual species ultracold neutral plasma and finding the value of the Coulomb logarithm in this strongly coupled regime.

Chapter 2

Methods

2.1 Magneto optical trap and ionization

Our first objective in creating a dual species plasma is to trap Ca and Yb neutral atoms. This is achieved by superimposing two magneto optical traps (MOT). A MOT consists of six circularly polarized laser beams intersecting in the middle of a magnetic quadrupole field [33]. The quadrupole field shifts the excited state energy levels of the atom when the atoms move from the center of the trap. The lasers excite the neutral atoms on the edge of the trap and provide state selective radiation pressure confining the atoms to the center of the trap.

The quadrupole magnetic field is formed using an anti-Helmholtz coil configuration. In traditional Helmholtz coils the magnetic field is produced by two coils oriented parallel to the $x - y$ plane carrying current in the same direction. The coils are displaced some distance from the origin in the $\pm z$ direction. The current through the coils produce a uniform magnetic field at the origin pointing in the z direction, as indicated by the right hand rule. This produces a field in which the magnetic field gradient is zero at the origin, $\nabla \mathbf{B} = 0$. In contrast, the anti-Helmholtz configuration contains no magnetic field at the center but which increases linearly with distance from the origin,
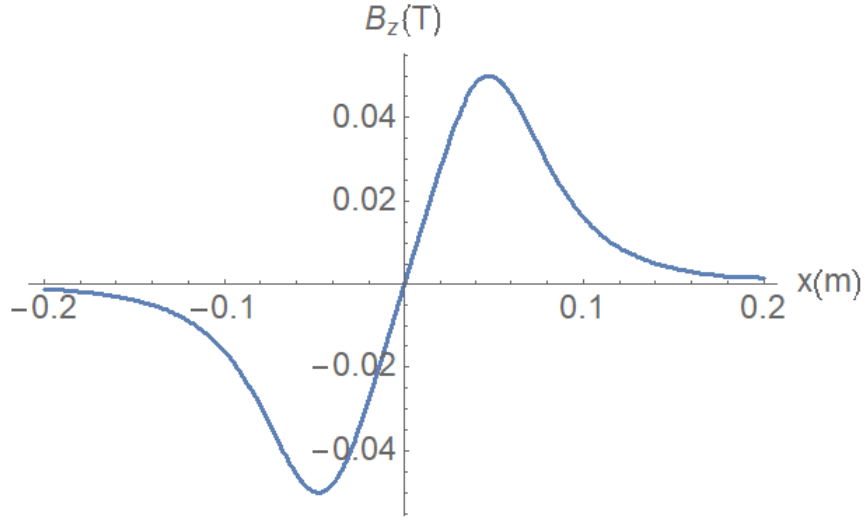
Figure 2.1 Represent magnetic field strength, Eq. 2.1, along the z axis due to the quadrupole magnetic field produced by anti-Helmholtz coils.

as shown in Fig. 2.1 and is given by,

$$B = \frac{1}{2}\left(I\mu_0 r^2\right)\left(\frac{1}{(r^2+(z-z_0)^2)^{3/2}} - \frac{1}{(r^2+(z+z_0)^2)^{3/2}}\right). \tag{2.1}$$

In this equation I is the current through the coil, μ_0 is the permeability constant in free space, r is the radius of the coils and z_0 is the displacement of the coils from the origin.

The presence of the magnetic field induces an energy splitting in the excited states of Ca and Yb, known as the Zeeman effect, as illustrated in Fig. 2.2. For Ca in the presence of a magnetic field, the energy splitting is represented by the Hamiltonian,

$$H = H_0 + V_{mag}(r) \tag{2.2}$$

where H_0 is the unperturbed Hamiltonian for the calcium atom in the absence of external fields and $V_{mag}(r)$ is the magnetic potential perturbation. By applying simple first order perturbation theory we can see that the presence of the magnetic field will induce an energy shift, to first order, of

$$\Delta E = \langle V_{mag}(r)\rangle = \mu_B m_j B_{ext}, \tag{2.3}$$
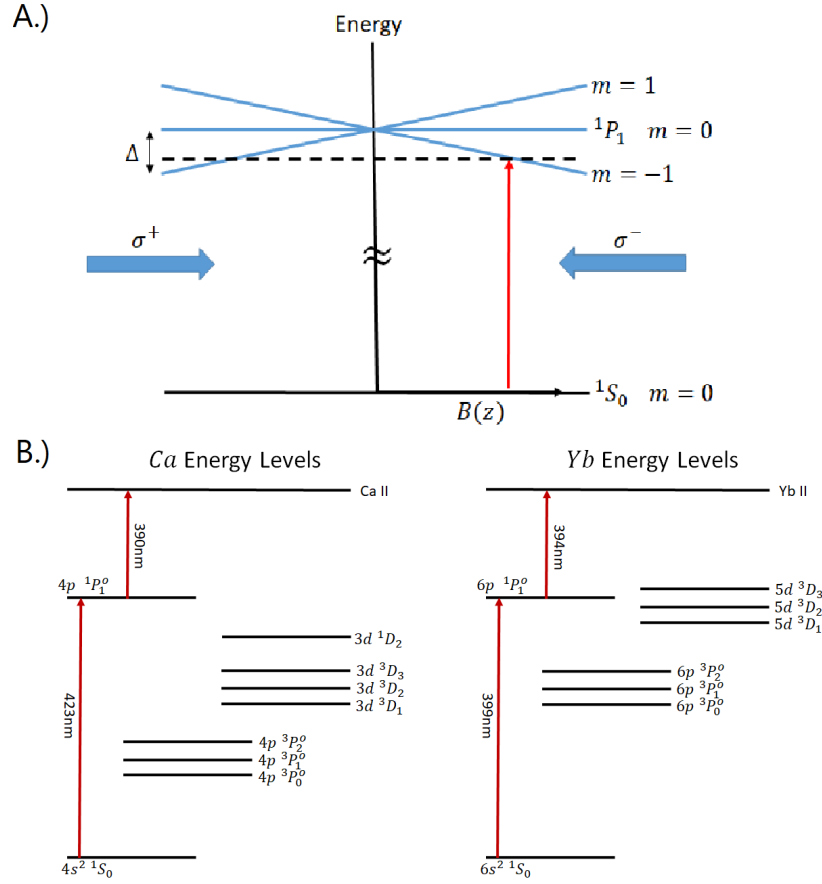
Figure 2.2 A: The energy splitting that occurs due to Zeeman splitting from a linear magnetic field. The $^1P_1$ state experiences energy splitting, $m = \pm 1$ in the presence of a magnetic field. The circularly polarized light from the MOT beam excites the neutral atoms and provides state selective radiation pressure that push the neutral atoms to the center of the magnetic quadrupole trap. B: This diagram shows the relevant energy levels for Ca and Yb. Laser beams at 423 nm for Ca and 399 nm for Yb are used for the MOT. Pulsed laser beams at 423, 390 nm and 399, 394 nm cause two photon excitation to the continuum, for Ca and Yb, respectively

where m_j is the magnetic quantum number, B_{ext} is the external magnetic field, and $\mu_B = \frac{e\hbar}{2m_e}$ is the Borh magneton. The energy splitting also occurs for Yb with a comparable magnitude [28–30], allowing us to trap both species in the same magnetic field.

Six laser beams at 399 nm and 423 nm intersect in the middle of the magnetic quadrupole field, as shown in Fig. 2.3. In Cartesian coordinates, there are two counter-propagating beams with
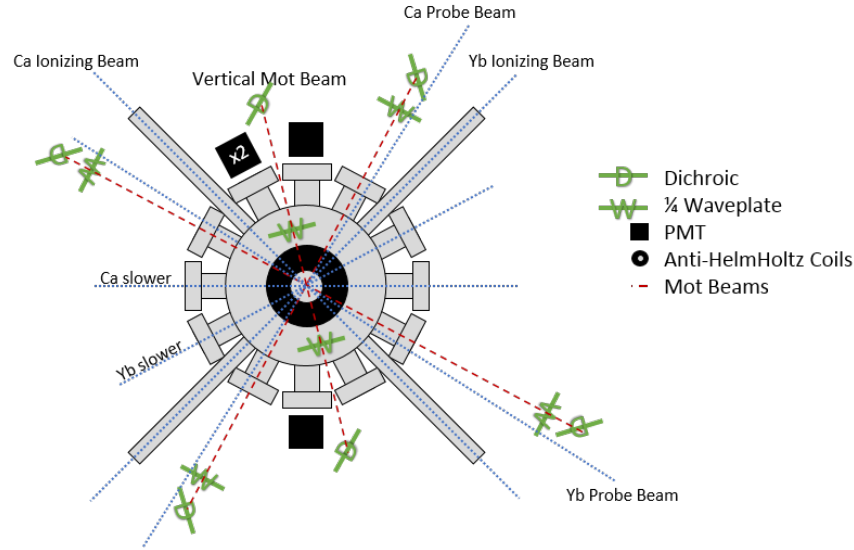
Figure 2.3 Diagram of the experimental apparatus. 6 Ca and Yb MOT beams at 423 nm and 399 nm, respectively, are overlapped in space by a 405 nm dichroic mirror (423 nm transmitted, 399 nm reflected). The beams pass through quarter waveplates that are aligned to give opposite polarization to the beams traveling in opposite directions along the same axis. The ionization beams for Ca and Yb are (423 nm,390 nm) and (399 nm,394 nm) respectively. The probe lasers are used to fluoresce the plasma at 397 nm for Ca and 370 nm for Yb. The photo multiplier tubes (PMT) are filtered to measure the energy relaxation of the plasma from the florescence.

opposing circular polarization on each axis for each atomic species. A 405 nm long-pass dichroic mirror transmits the 423 nm laser beam and reflects the 399 nm laser beam providing spatial overlap of the Yb and Ca Beams. These laser beams excite the $4s^2\ ^1S_0 \rightarrow 4s4p\ ^1P_1^o$ transition for Ca and $6s^2\ ^1S_{1/2} \rightarrow 6s6p\ ^1P_1^o$ transition for Yb.

If the Lande g-factor is 1 then the Zeeman energy shift is 1.4 MHz/G. If the magnetic field gradient is 100 G/cm then the quadrupole magnetic field shifts the atomic energy levels for the $m_j = \pm 1$ in the $^1P_1$ state by 14 MHz at $r = 1$ mm. Circular polarization provides state selective radiation pressure, resulting in a force that pushes the atoms to the center of the trap, as shown in Fig. 2.2.

The atoms are supplied by heating up metal pieces of Yb at 430 °C and Ca at 500 °C. At

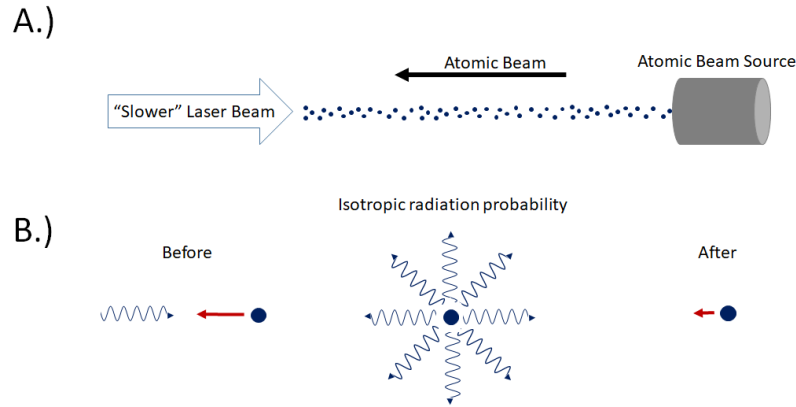**Figure 2.4** A: The atomic beam is created through collimation of the atoms so that only a directional velocity is selected. These atoms are then slowed by means of Doppler cooling. B: Illustrates the process of Doppler cooling. The atoms that are Doppler shifted above resonance will absorb photons from the slower beam. The photon can then radiate in any direction. On average the atom will emit the photon in the opposite direction resulting in a momentum transfer that slows the atom down, as indicated by the magnitude of the red arrows.

these temperatures the metals sublimate. Collimation micro tubes are used to select the atoms that are moving towards the MOT, forming an atomic beam [32]. The majority of the atoms in the atomic beam have too much kinetic energy to be trapped. We slow the atoms down using a counter propagating laser beam as illustrated in Fig. 2.4. The laser beam is detuned $-250\,\text{MHz}$ from resonance. As the atoms enter the trap they are continuously being laser-cooled while the trap supplies state selective radiation pressure confining the neutral atoms to the center of the trap.

Once the atoms are trapped, we photo-ionize them using a Nd:YAG-pumped pulsed dye laser. For Ca we use 3 ns laser pulses at 423 nm and 390 nm to excite the Ca atoms to the Ca^+ ground state. Likewise in Yb, we use 7 ns laser pulses at 399 nm and 394 nm to excite the Yb atoms to the Yb^+ ground state, as shown in Fig. 2.2. Once the atoms are ionized, the plasma is no longer confined by the MOT and starts expanding. The expansion and evolution of the plasma contains information about the electron temperature, ion temperature, equilibration rates, ion-ion friction and the Coulomb logarithm.

2.2 Probing techniques

Information about the neutral atoms and the ions can be extracted using laser induced fluorescence and absorption. Probing the neutral atoms and ions provide empirical measurements that are used in determining the neutral atom and ion cloud densities, plasma expansion, equilibration rates, ion-ion friction and the Coulomb logarithm. Using absorption we determine the size and density of the neutral atom cloud trapped in the MOT. Laser induced fluorescence tells us the relative number of atoms ionized and in turn gives us the initial ion cloud density. Laser induced fluorescence is also used to measure the expansion of the plasma in real time.

The neutral atom cloud density of Ca and Yb is determined using absorption. A weak laser beam on resonance illuminates the neutral atoms within the MOT. The atoms absorb the photons and emit them isotropically. The Gaussian laser beam profile has a dark spot in the middle when the MOT atoms are present, compared to when they are absent. The ratio of the two background subtracted laser beam images tells us the percentage of photons absorbed,

$$100 \left(1 - \frac{F_{abs} - F_{MOT}}{F_{laser} - F_{dark}} \right) = \%\text{Absorption}, \tag{2.4}$$

where F_{abs} is the absorption signal, F_{MOT} is the signal of only the trapped atoms in the MOT, F_{laser} is the signal from the laser beam and F_{dark} is the background signal with no trapped atoms and no absorption laser beam present. This is visualized in Fig. 2.5. Using Beer's Law, we determine the peak density by,

$$\frac{dI}{dz} = -I\sigma n \tag{2.5}$$

where I is the intensity of the laser beam, σ is the absorption cross section of the atoms and n is the density. Assuming a Guassian density profile with an rms width of r_0 and peak density n_0, we can write,

$$\ln \left(\frac{I_f}{I_0} \right) = \int -\sigma n_0 \exp(-z^2/2r_0^2)dz. \tag{2.6}$$
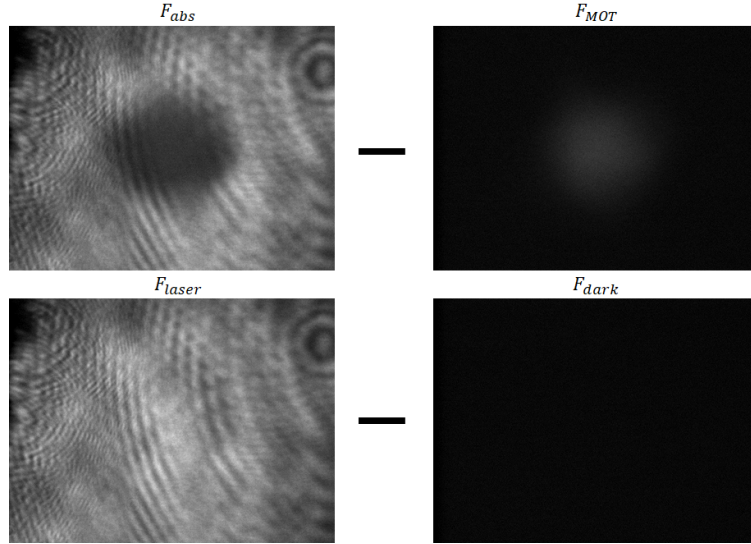
Figure 2.5 Demonstrates pictorially how the absorption measurement is taken, analogous to Eq. 2.4. Image F_{abs}: This is an image of absorption of the MOT. Image F_{MOT}: This is an image of the fluorescence of the MOT. Image F_{laser}: This is an image of the laser beam used to make the absorption measurement. Image F_{dark}: This is an image of the background.

In this equation I_0 is the intensity of the laser beam prior to interacting with the neutral atoms and I_f is the intensity of the laser beam after interacting with the neutral atom. Solving for the peak density, n_0, we get

$$n_0 = \frac{1}{\sigma r_0 \sqrt{2\pi}} \ln\left(\frac{I_0}{I_f}\right). \tag{2.7}$$

Using r_0 as a fit parameter of the absorption image to a two dimensional Gaussian, we find the size and density of the neutral atom cloud. A typical size and density for our trapped neutral atoms are 300 μm and 10^{10} /cm^3 respectively.

Beer's law works under the assumption that the atoms are not influenced or stimulated by other light sources. If the MOT density is low enough, on the order of 10^{10} /cm^3, we can assume the lasers associated with the MOT do not perturb the absorption measurements in any measurable way. If the density is too high our absorption measurements are no longer reliable. As an alternative we detune the frequency of the absorption beam from resonance and use the Lorentzian line shape for
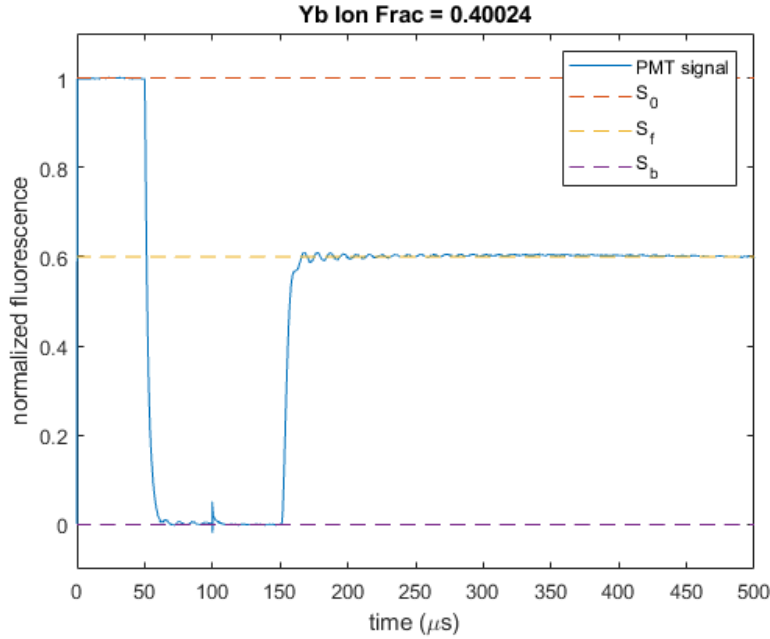
Figure 2.6 This is a plot of the normalized, background subtracted, neutral Yb fluorescence signal as a function of time. Initially there are no ions so our signal, S_0, is from the MOT. The MOT beams are blocked at time $t = 0.5$ and the background is measured, S_b. Then the ionization pulses ionize the Yb atoms and the MOT fluorescence is measured, S_f. Use in reference with Eq. 2.10.

Ca, $\Gamma = 35$, and Yb, $\Gamma = 28$, to correct the measurement. The absorption cross section is given by,

$$\sigma = \frac{3\lambda^2}{2\pi} \frac{1}{1 + (2\Delta/\Gamma)^2}, \tag{2.8}$$

where Δ is the detuning from resonance, λ is the wavelength and Γ is the FWHM. The ratio of on resonance, $\Delta = 0$, to off resonance will provide a scaling factor for the density,

$$n = n_{\text{off}} \left[1 + (2\Delta/\Gamma)^2 \right], \tag{2.9}$$

where n_{off} is the density found off resonance and n is the true density.

Both the ion density and the ion expansion are determined by laser induced fluorescence. A probe laser tuned to 397 nm and 369 nm for Ca^+ and Yb^+ respectively is used to fluoresce the ions. The fluorescence is then measured using two photo multiplier tubes (PMT) that are optically

filtered to the respective wavelengths for Ca^+ and Yb^+. They can be used to tell us how the plasma is evolving in time. A second set of PMT's, one optically filtered at 423 nm for Ca and the other at 399 nm for Yb, is used to track the number of trapped neutral atoms as a function of time. Before the ionizing pulses come in, all the atoms are in the trap. Once the neutral atoms are ionized they no longer fluoresce at 399 nm and 423 nm, for Ca and Yb respectively. The difference in the background subtracted fluorescence signal before and after the ionizing pulses give us an ionization fraction, which we use to scale the trapped neutral atom density to give us the ion density,

$$n_{ion} = \left(1 - \frac{S_f - S_b}{S_0 - S_b} \right) n. \tag{2.10}$$

In this equation n_{ion} is the ion density, S_0 is the PMT signal before the ionizing pulse, S_f is the PMT signal after the ionizing pulse, S_b is the background signal and n_0 is the neutral atom peak density, also illustrated in 2.6. Typical ionization fraction for Ca and Yb are 99% and 50% respectively.

2.3   Timing and control

In 2005 Theodor W. Hansch and John L. Hall shared the Nobel prize for their invention of the optical frequency comb [44]. We reproduce their frequency comb in our lab. It serves as an ideal reference for control, such as; continuous wave (CW) laser frequency stability and frequency scanning for fluorescence measurements.

One of the most important controls is that of laser frequency stabilization. Frequency shifts on the order of 1-10 MHz results in measurable differences in the number of atoms trapped and the size of the trapped atom cloud. The frequency comb provides a reference for stabilizing laser frequencies to the 10 kHz level. An integral feedback lock circuit locks the frequency comb and CW laser beat note to a variable control frequency generator [41]. Feedback control can be illustrated using a simple schematic, as shown in Fig. 2.7. A controller transfers an input voltage to a laser frequency. The frequency is compare to the desired frequency and the difference influences the
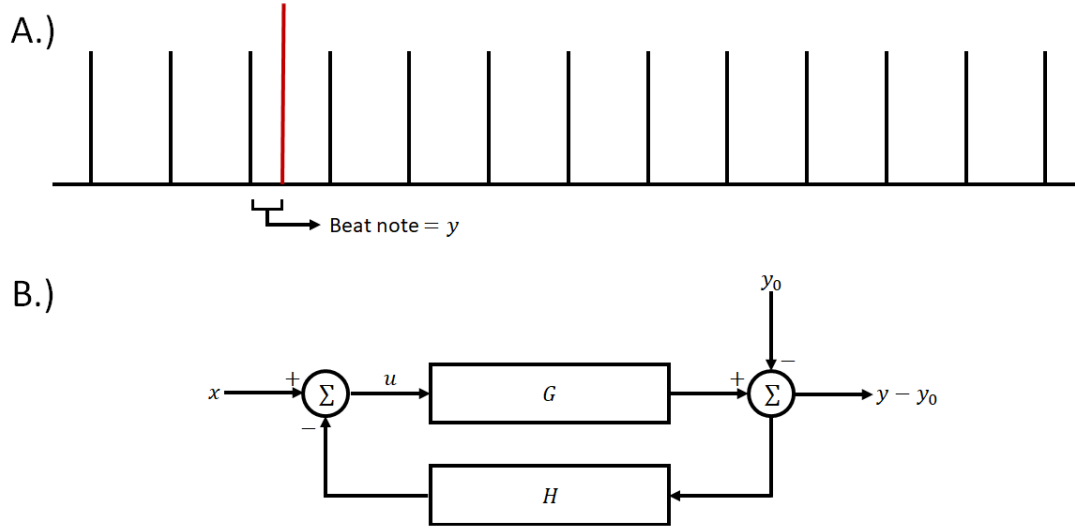
Figure 2.7 A: Illustrates the beat note between the frequency comb and the fundamental frequency of the MOT laser beam. This beat note is used to lock to the desired frequency. B: A block diagram of a simple integrated lock circuit. A mathematical representation is shown in Eq. 2.11-2.13. $x =$ control voltage, $G =$ controller, $y =$ laser beatnote, $y_0 =$ desired beatnote, $H =$ feedback controller.

controller input. Referring to Fig. 2.7 we find,

$$y = Gu \tag{2.11}$$

$$u = x - H(y - y_0) \tag{2.12}$$

which gives,

$$y = \frac{Gx + GHy_0}{1 + GH}. \tag{2.13}$$

In this equation y is the beat note, y_0 is the desired beat note set by a frequency generator, x is the input voltage on the laser controller, G is the controller transfer function and H is the feedback gain on the lock circuit. The comb is stable to the 10 kHz level. When locked, the frequency generator, y_0, allows us to make fine adjustments to the laser frequency. This method of locking to the comb is used for the MOT laser beams, ion fluorescence probes and optical pumping lasers.

For Ca and Yb a Nd:YAG pulse laser is used for ionizing the atoms. Laser beam pulses at

846 nm and 798 nm, for Ca and Yb respectively, are amplified by means of harmonic generation though a double pass dye laser and then frequency doubled to 423 nm and 399 nm. Another pulse is sent through a dye laser cavity where 390 nm and 394 nm wavelengths are resonant for Ca and Yb respectively. By adjusting the cavity length of the dye lasers we can control the wavelength of the laser that drives the $4s4p$ $^1P_1$ (Ca) and $6s6p$ $^1P_1$ (Yb) to continuum transitions. The dye laser cavity length in turn controls the electron temperature. The energy of the pulse above the continuum limit is proportional to the electron temperature,

$$\frac{3}{2}k_B T_e(0) = h\nu - E_{continuum},$$
(2.14)

where k_B is Boltzmann's constant, $T_e(0)$ is the initial electron temperature, h is Plank's constant, ν is the sum of the frequencies of the ionizing lasers and $E_{continuum}$ is the threshold energy for ionization. The electron temperature drives the expansion of the ions by means of the ambipolar field,

$$a_i(r,t) = -\frac{k_B T_e(t)}{m_i} \frac{\nabla n_t(r,t)}{n_t(r,t)},$$
(2.15)

where m_i is the ion mass and n_t is the total plasma density. Increasing the electron temperature increases the rate at which the plasma expands. As we will see later in section 2.5, this control allows us to map out the Coulomb logarithm of a dual species plasma as a function of the electron temperature.

The timing for the ionization of the neutral atoms is controlled using a pulse generator. Since we are dealing with pulses, instead of CW laser beams, timing matters. Our pulse lasers create approximately 5 ns pulses which translate to about 1.5 m long pulses of light. For Ca, the 423 nm and 390 nm ionizing pulse laser beams are incident with the MOT at the same time. The pulses need to be overlapped in time in order to achieve two photon ionization. The same is done for the 399 nm and 395 nm Yb ionizing pulses. We control the relative Ca^+ and Yb^+ plasma formation to ± 2 ns by controlling the trigger delay for each set of pulses.

Unfortunately the 390 nm pulse laser for Ca ionizes excited Yb atoms and the 394 nm pulse
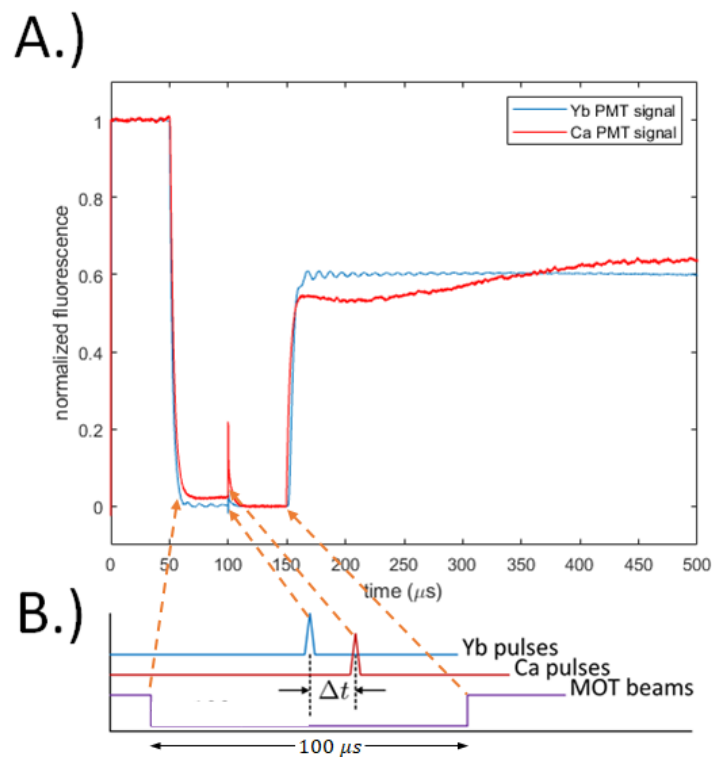
Figure 2.8 A: In this figure we see the Ca (blue) and the Yb (black) fluorescence signals as functions of time. We can see that in both cases at time $t = 50\ \mu$s the AOM for Ca and EOM for Yb perturbed the MOT beams off the atoms, and at time $t = 150\ \mu$s Yb and Ca are ionized. B: This shows the timing of the experiment. The MOT beams are shut off $100\ \mu$s prior to ionization and the Ca pulse is delayed some Δt after Yb.
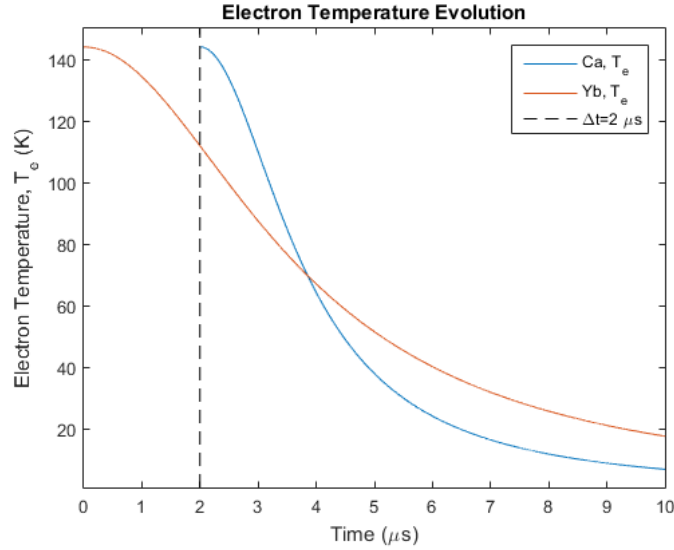
Figure 2.9 This graph illustrates what can happen if the Ca ionizing pulse is delayed 2 μs without correcting for the electron temperature evolution. In this case there will be extra heating of the ions due to electron thermalization.

laser for Yb ionizes excited Ca atoms. This is referred to as cross-ionization. This introduces a problem because the electron temperature is determined by the energy of the pulse above the ionization limit, and the expansion of the plasma is determined by the electron temperature. Cross ionization complicates our control of the electron temperature and therefore the plasma expansion. This problem is fixed by turning off the MOT beams 100 μs prior to the ionizing pulses and delaying the pulses by some Δt relative to one another, with Yb ionizing first. Turning off the MOT beams is achieved using an acousto optical modulator and an electro optical phase modulator. As shown in Fig. 2.8, the electron temperature changes as the plasma expands, and if the two plasmas are not ionized simultaneously then the electron temperatures will not be the same at time $t = \Delta t$, as shown in Fig. 2.9. The electron evolution is determined by [7],

$$T_e(t) = T_e(0)\frac{1}{1+t^2/\tau^2}, \tag{2.16}$$

where $T_e(0)$ is the initial electron temperature and τ is the characteristic expansion time [31],

$$\tau_{exp} = \sqrt{m_i \sigma(0)^2 / k_B [T_e(0) + T_i(0)]}. \tag{2.17}$$

In this equation m_i is the mass of the ion, $\sigma(0)$ is the initial absorption cross section and k_B is Boltzmann's constant. There are two ways we can fix the inequality of the electron temperatures. First, we can delay Ca^+ by a small amount, $\Delta t = 40$ ns. At short time delays the electrons have not had enough time to cool and are essentially the same temperature as when the plasma was first formed. Second, we could increase the initial electron temperature of Yb^+ so that at time Δt it is equal to the electron temperature of Ca^+. The electron temperatures for Ca^+ and Yb^+ are chosen such that at time Δt they have equal electron temperatures. This ensures there is no extra heating or cooling due to thermalization of the electrons.

Once the plasma is formed, laser induced fluorescence is used to probe the ionization fraction as well as the expansion. The pulse laser intensity contributes to the ionization fraction. Attenuation of the pulse laser results in a smaller ionization fraction. This gives us control over the ion density for both Ca and Yb. For this experiment we are interested in a Yb/Ca ion density ratio of 1. In future work we hope to use this control to probe much large and smaller fractions of the ion density.

Ion expansion is observed by scanning the frequency of 370 nm and 397 nm lasers for Ca^+ and Yb^+ respectively, as shown in Fig. 2.10. The probe beam frequency is offset-locked to the optical frequency comb and controlled using an RF generator [41]. We can detune the second harmonic probe beam from the resonant frequency by ±360 MHz. Different velocity classes of atoms will become Doppler-shifted into resonance with the probe beam at different laser frequencies. This allows us to velocity select, projected in the direction of the beam propagation, which atoms we wish to probe. We scan the plasma in 30 MHz increments and measure the expansion as a function of time. The intensity of the probe beam controls how much signal we get from the ions. Higher intensities introduce unwanted dark state transitions. For this reason the probe intensity is set to be
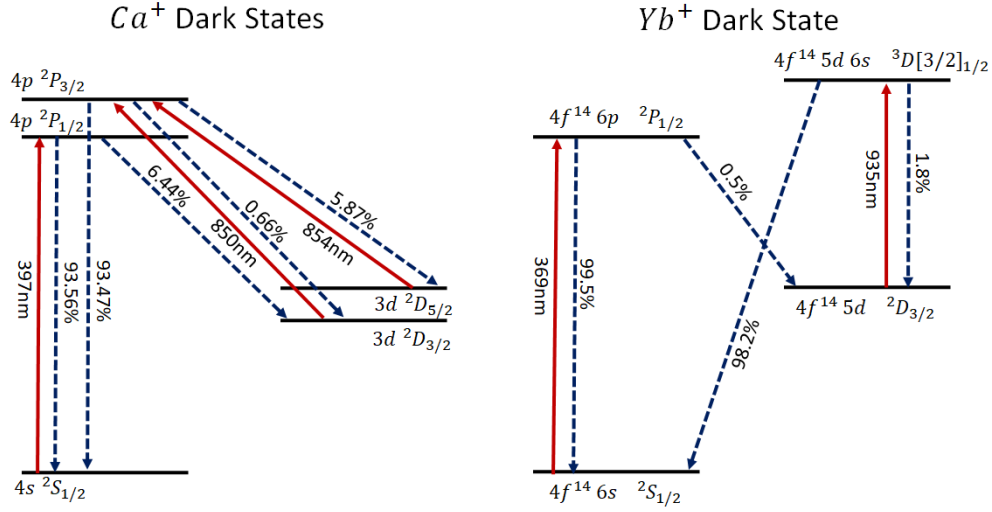
Figure 2.10 This diagram shows the relevant atomic transitions for Ca$^+$ and Yb$^+$. The laser induced fluorescence probes and the optical pumping excitation beams are indicated with red arrows, and the respective wavelength to the left of the respective arrow. The possible decays from each state are given as dashed blue arrows with the respective branching fractions to the right [39].

about 10% of the saturation intensity I_{sat},

$$I_{sat} = \frac{\pi h c}{3\lambda^3 \tau},$$ (2.18)

where h is Planks constant, c is the speed of light in vacuum, λ is the wavelength and τ is the lifetime of the excited state. The saturation intensity is defined by the intensity needed to have 50% of the atoms or ions in the excited and ground states. Operating at a fraction of the saturation intensity allows the atoms to spend less time in the excited state which means less of a chance of falling to dark states.

Dark states are metastable atomic states in the ion that do not interact with the ion probe laser beam. To measure the expansion of the plasma we fluoresce the ions. As long as the ions fall back into the respective ground states they can continue to be excited by the probe laser beams. In Ca$^+$, the ions are excited to the $4p\,^2P_{1/2}$ state. From the $4p\,^2P_{1/2}$ state the ions will fall to either the ground state, $4s\,^2S_{1/2}$, or to the $3d\,^2D_{3/2}$ dark state, with branching fractions of 93.56% and 6.44%

respectively [37]. The ions that end up in the $3d\,^2D_{3/2}$ dark state are excited to the $4p\,^2P_{3/2}$ state using a laser beam at 850 nm. 93.47% of these ions will fall to the ground state, $4s\,^2S_{1/2}$, while the remaining will fall to either the $3d\,^2D_{3/2}$ or $3d\,^2D_{5/2}$ dark states, with branching fractions of 0.66% and 5.87% respectively [38]. For Yb$^+$ ions, there is only one dark state, $5d\,^2D_{3/2}$. Similar to Ca$^+$, Yb$^+$ can be optically pumped using a laser beam at 935nm, where all the relevant states and branching fractions for Ca$^+$ and Yb$^+$ are shown in Fig. 2.10. If we operate at a fraction of I_{sat} and are only interested in the first 5 μs of expansion we can safely neglect the Yb$^+$ $5d\,^2D_{3/2}$ and the Ca$^+$ $3d\,^2D_{5/2}$ dark states.

2.4 Geometrical considerations

It is important to understand the geometry of our experiment so that we can understand which measurements we are taking. There are a number of things that need to be considered such as: MOT spatial overlap and shape, probe beam size vs plasma size, and how time and timing effects the geometry. Controlling these aspects allow us to observe dual species plasma expansion in an ideal setting.

One of the most challenging aspects of the experiment is the Ca and Yb MOT overlap and shape. We have constructed a 6 beam MOT for both the Ca and Yb neutral atoms. The 6 beam configuration gives us control over the MOT placement and shape. If we view the beam configuration in Cartesian coordinates then the beams will be counter-propagating along the 3 coordinate axes. We can control the position of the MOT by adjusting the power balance between the counter propagating beams. For example, we can move the trapped atoms in the positive x direction by increasing the power in the x_+ beam and decreasing the power in the x_- beam, as shown in Fig. 2.11.

If the beam profile was a perfect Gaussian we would have a perfectly spherical MOT. This is not the case. The laser beam profile that couples out of the laser cavity is astigmatic. Also diffraction is
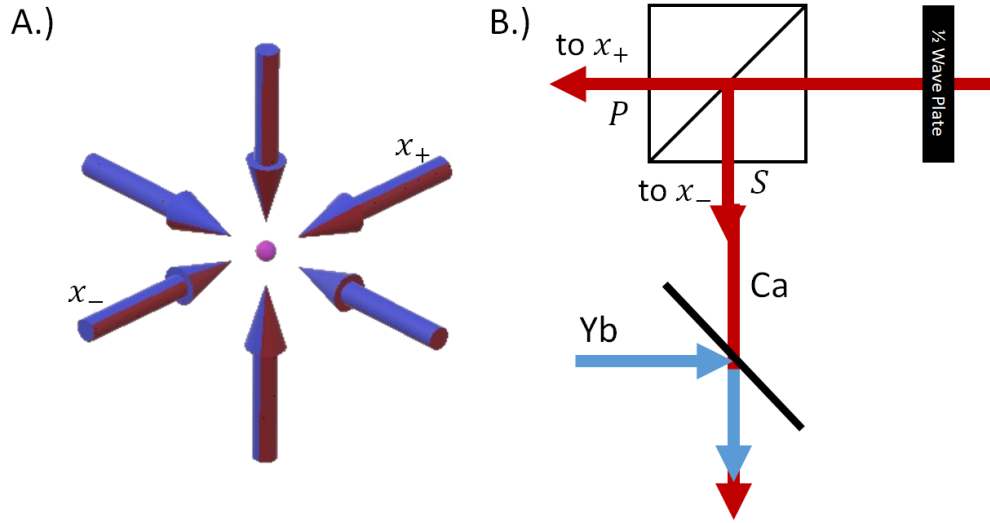
Figure 2.11 A: Diagram of the MOT laser beams. B: The MOT laser beam passes through a 1/2 waveplate and is split using a polarizing beam splitter. This makes up the coaxial counter propagating laser beams shown in A. The power balance between the two beams is controlled by rotating the 1/2 waveplate. The Yb and Ca MOT beams are overlapped in space using a dichroic mirror.

introduced when passing through polarizing beam splitter cubes, modulators and apertures. These effects contribute to structure in the MOT. We correct for MOT shape by adjusting the pointing of the 6 MOT beams until the overlap is near perfect and the shape can reasonably be approximated as a Gaussian. We confirm the shape and overlap by observing the fluorescence of the MOTs from two different angles, as shown in Fig. 2.12. We then further help smooth-out the structure by shutting off the MOT beams 100 μs before ionization. This allows the Ca and Yb atoms to move around and average out the structure to give us a more Gaussian looking profile at the expense of about 12% decrease in the Ca density and 3% decrease in Yb density.

Once the dual species MOT overlap and shape problems are solved we then probe the ions. We want to see how Yb$^+$ influences Ca$^+$ expansion. In order to do this we need to consider the size of the probe beam that fluoresces the plasma. A typical plasma in our experiment, initially, is on the order of 300 μm. We are interested in observing the expansion for 5 μs. This puts a lower limit on
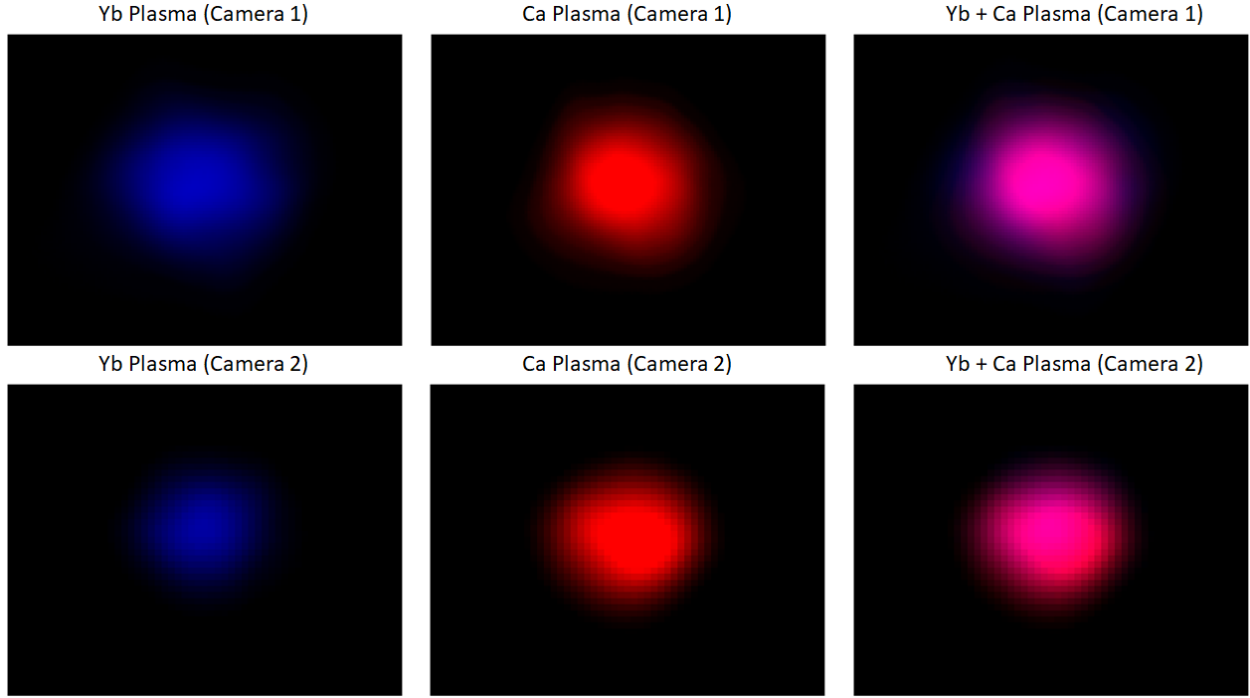
Figure 2.12 False color images of the MOT fluorescence. The first row of images is from camera 1 while the second row is camera 2. The two cameras collect images from different angles to verify MOT shape and overlap. The first two columns show typical MOT shapes for Yb (blue) and Ca (red). The last image in each row is a superposition of the first two images to show the Ca/Yb MOT overlap.

the size of our probe beam. If we look at the asymptotic behavior of the expansion, Eq. 2.20, at long times we find that,

$$v_{i,rms} = c\sqrt{\frac{k_B T_e(0)}{m_i c^2}} \tag{2.19}$$

where $T_e(0)$ is the initial electron temperature, k_B is Boltzmann's constant, $m_i c^2$ is the rest mass energy of the ions and c is the speed of light. If we let $k_B T_e(0) = 0.035\text{eV}$, corresponding to 400 cm^{-1} above ionization threshold, and the ion mass energy of Ca is 40 GeV, then we get $v_{i,rms} = 280$ m/s. Giving an expansion of 2.8 mm. If we want to observe all the ions for 10μs then the beam size needs to be about double this value. Limiting the beam size of the probe laser limits how far out in time we can look.

2.5   Analysis and modeling

Analysis and modeling of the raw data provide insights on one of two things, what we are doing wrong or the physics of the experiment. It is important to have a "check" to ensure that we are not measuring an artifact or some other mistake. For this purpose, single species expansion data is taken and verified with the known Vlasov model. Once the analysis is complete a particle in cell (PIC) model with friction is used to understand the physics by comparing with the experimental data.

The PMT's produce a current that is proportional to the number of photon counts per second as a function of time. We take this information and represent it as plasma expansion. How this is done will be more thoroughly addressed in chapter 3. It will suffice to say that there are several steps to the analysis that help us understand and represent the evolution of our Yb^+/Ca^+ dual species plasma.

Single species plasma dynamics are exactly realized in the Vlasov equation [31], with the expansion velocity given as

$$v_{i,rms} = \sqrt{\frac{k_B}{m_i}\left\{\frac{t^2}{\tau_{exp}^2}[T_e(t)+T_i(t)]+T_i(t)\right\}}. \tag{2.20}$$

In this equation τ_{exp} is the characteristic expansion time given in Eq. 2.17, T_i and T_e denote the ion and electron temperatures found in Eq. 2.16 and m_i is the ion mass. The rms size of a single species plasma evolves according to

$$\sigma^2(t) = \sigma^2(0)(1+t^2/\tau^2), \tag{2.21}$$

where $\sigma(0)$ is the initial plasma rms size. During data collection, single species and dual species expansion data are taken. This provides a way for us to indirectly check our work by making sure the single species data matches the known Vlasov solution as shown in Fig 2.13. We represent all data on a velocity vs time plot, which represents the characteristic plasma expansion.

In a dual species plasma the Vlasov equation fails. The Vlasov equation assumes collisions do not change the velocity distribution. This is not true for a dual species plasma because the two
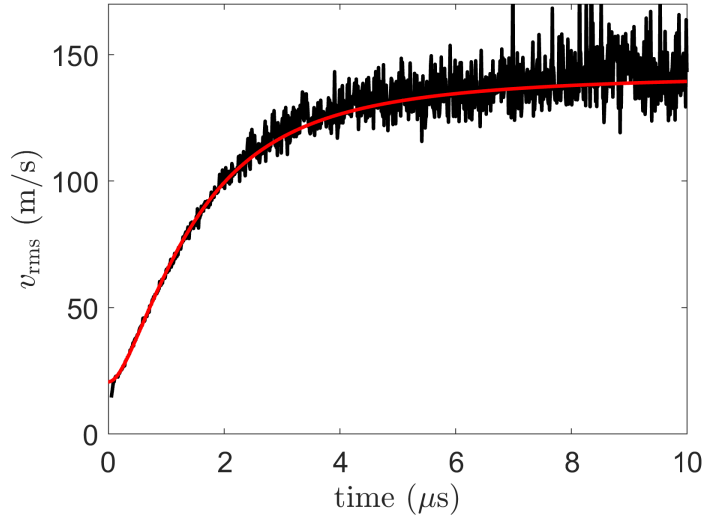
Figure 2.13 This is a plot of the experimental Ca^+ plasma expansion (black) compared with the expansion predicted by Vlasov's equation (red).

plasmas are coupled together and experience ion-ion friction forces. The next step in the analysis is to generate a model that explains the relevant physics and matches experimental data.

For a single species plasma we know that the expansion is driven by the ambipolar field, given by Eq. 2.15. Assuming a Gaussian density profile for a single species plasma, this can be simplified down to,

$$a_i(r,t) = \frac{k_B T_e(t)}{m_i} \frac{r}{\sigma^2(t)}.$$

(2.22)

In this equation $\sigma(t)$ is the plasma size and r is the distance from the center of the plasma. The ambipolar field acceleration can be modeled very nicely with the adoption of a particle in cell (PIC) method.

PIC is ideal when the driving force between particles cannot be cut off due to an inverse square law. Since our driving force is linear in r the PIC method is a good platform to build from. The electrons exert a force on the ions described by the ambipolar field, Eq. 2.15. Compared to the alternative of MD simulations, where every ion and electron interact through some Yukawa or Coulomb potential, we have a field that acts on all the ions. This is the beauty of PIC, it cuts down
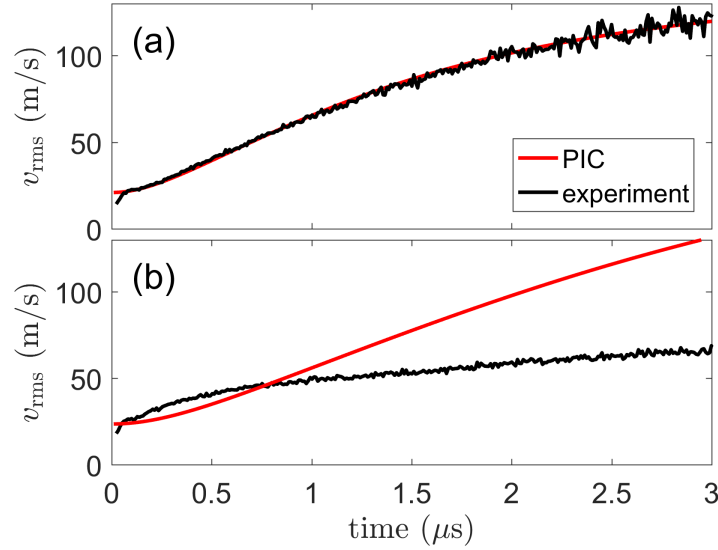
Figure 2.14 In both figures, black represents experimental data and red show the results predicted by the PIC model. (a) Shows the success of the PIC model for a single species plasma, Ca^+. Where the expansion In PIC is driven by the ambipolar field, Eq. 2.22. (b) Demonstrates the failure of treating the expansion of a dual species plasma using only the ambipolar field, Eq. 2.23.

the number or computations from N^2 to N and still maintains the relevant physics. It is shown in Fig. 2.14 that this treatment of the electrons follows the experimental data for a single species plasma.

In a dual species plasma the expansion is much more complicated. The ambipolar field contains terms that make the Valsov equation analytically unsolvable,

$$a_i(r,t) = \frac{k_B T_e(t)}{m_i} \left(\frac{n_{Ca} \frac{r}{\sigma_{Ca}^2} \exp\left[\frac{-r^2}{2\sigma_{Ca}^2}\right] + n_{Yb} \frac{r}{\sigma_{Yb}^2} \exp\left[\frac{-r^2}{2\sigma_{Yb}^2}\right]}{n_{Ca} \exp\left[\frac{-r^2}{2\sigma_{Ca}^2}\right] + n_{Yb} \exp\left[\frac{-r^2}{2\sigma_{Yb}^2}\right]} \right). \tag{2.23}$$

We also realize that if we only include this acceleration term in a PIC model it fails to describe the evolution, Fig. 2.14. The failure suggests there is more to the picture than just the ambipolar field. Ion-ion interactions are included by having the fluid flow of Yb^+ influence the Ca^+ ions,

$$F_{12} = -\mu n_2 \pi \left(\frac{e^2}{2\pi\varepsilon_0\mu}\right)^2 \frac{(v_1 - \langle v_2 \rangle)}{|v_1 - \langle v_2 \rangle|^3} \Lambda, \tag{2.24}$$

where v_1 is the Ca$^+$ ion velocity for each ion, $\langle v_2 \rangle$ is the hydrodynamic flow of the Yb$^+$ ions collectively at the location of the Ca$^+$ ion, n_2 is the density of Yb$^+$ at the location of the Ca$^+$ ion, μ is the reduced mass of Ca and Yb, e is the fundamental unit of charge, and ε is the permittivity in free space. The Coulomb logarithm, Λ, is used as a constant. This treatment of the friction force preserves Newton's third law for fluids and is consistent with the plasma formulary [2,40]. One may notice that under the condition where $v_1 = \langle v_2 \rangle$ there is a singularity. This is corrected by adding in the thermal velocity from disorder induced heating in quadrature, where the disorder induced heating is given by [27],

$$v_{dih} = \sqrt{\frac{k_B T_{dih}}{m_i}}, \tag{2.25}$$

with

$$T_{dih} = \left(\frac{1}{\Gamma}\right)\frac{2}{3}\frac{e^2}{4\pi\varepsilon_0 a_{ws} k_B}. \tag{2.26}$$

In this equation Γ is the strong coupling parameter given by Eq. 1.1. Using Eqs. 2.23 and 2.24 to evolve the Ca$^+$ ions in time we can compare the model and experiment by choosing a value for the Coulomb logarithm. This allows us to extract a value for the Coulomb logarithm in the strongly coupled regime.

Chapter 3

Results

3.1 Introduction

Through comparison and contrast of the model to experimental data we we learn about the physics of our dual species plasma. We analyze the known behavior of a single species plasma as well and the unknown behavior of a dual species plasma. The single species plasma acts as a guide for verifying each step of the analysis for the dual species plasma. Unlike that of a single species plasma, the dual species plasma is observed to have ion collisions that change the velocity distribution function. The ion collisions are modeled as a fluid friction force to the Ca^+ plasma evolution. We are able to extract the Coulomb logarithm, Λ, in the strongly coupled regime for a Ca^+/Yb^+ density ratio of 1 by comparing to a PIC numerical model.

3.2 Experimental analysis

The PMT photo-current can be analyzed to tell us nearly everything we need to know about the dual species plasma. Building off chapter 2 section 5, we represent the data in many forms to gain intuition about the behavior of the plasma. The analysis provides information about the plasma
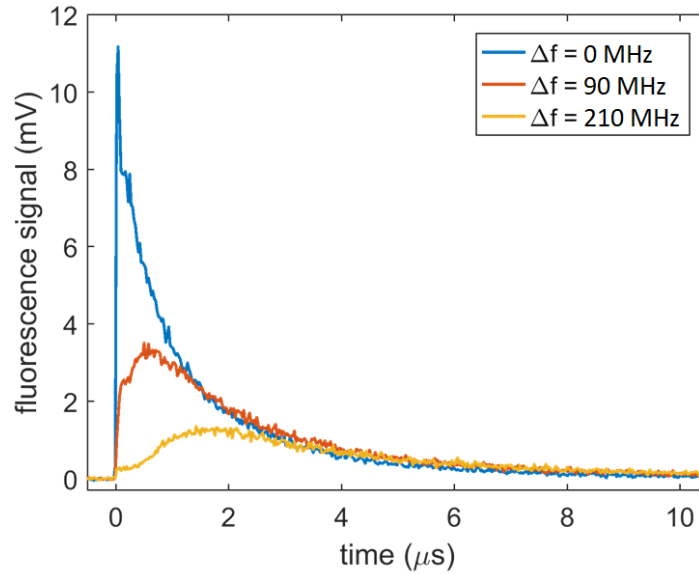
Figure 3.1 The fluorescence signal measured by a PMT as a function of time. Each frequency detuning from resonance measures a specific velocity class of the plasma expansion.

expansion and is compared to the results of a PIC model.

Stepping the frequency of the 394nm probe laser for Ca^+ and measuring the ion fluorescence as a function of time provides 3-dimensional data for understanding the plasma evolution. In Fig. 3.1, we represent the ion fluorescence in a signal strength vs time plot. This representation tells us relatively how many ions are Doppler shifted into resonance with the Ca^+ probe laser beam. When the neutral atoms are trapped in the MOT there is no Coulomb potential and virtually no collisions. The atoms are very cold, ≈ 1 mK, with very little kinetic energy. Once the neutral atoms are ionized they still have the same kinetic energy but now we have a Coulomb interaction between the cold ions. This causes a rapid heating and thermalization known as "disorder induced heating" [27]. Initially the plasma is stationary but the ions accelerate outward as they gain kinetic energy from the ambipolar field. If our probe laser is on resonance, then the zero velocity class ions are fluoresced. The peak fluorescence is at $t = 0$ and decays as the plasma's average ion velocity increases, as can
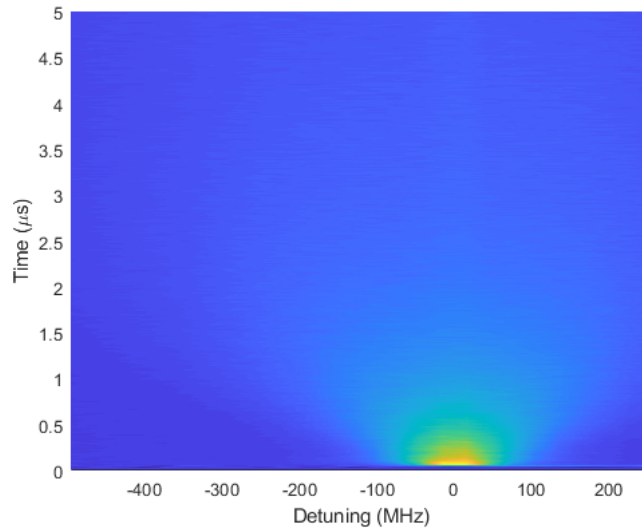
Figure 3.2 Similar to Fig. 3.1, this false-color plot shows the time vs. detuning for the first 5 μs of the plasma expansion. The color indicates the fluorescence signal, yellow representing high signal and dark blue representing low signal.

be seen in Fig. 3.1. Likewise if the probe laser beam frequency is detuned by some amount, Δ, then we expect less fluorescence initially. As the ions accelerate, we see an increase in the fluorescence as more ions become Doppler-shifted into resonance with the probe laser beam. Then the fluorescence decreases again as the average ion velocity continues to increase as, seen in Fig. 3.1.

We represent the ion fluorescence as a function of time and frequency using a false-color plot, with the color being the fluorescence signal, as shown in Fig. 3.2. The fluorescence indicates the relative number of ions at a given velocity at a particular time. This figure only represents the component of velocity along the propagation direction of the laser beam. The false color plot represents the plasma velocity (x) and ion number (color) as a function of time (y). The false color plot provides a good visualization of how the plasma expands. We do this for Ca^+ in the presence of Yb^+ and also Ca^+ by itself. In Fig. 3.3 we can see that for the case of $Ca^+ + Yb^+$ the expansion is slower than Ca only.

The velocity is extracted from the Doppler-broadened atomic line shape. The atomic line shape
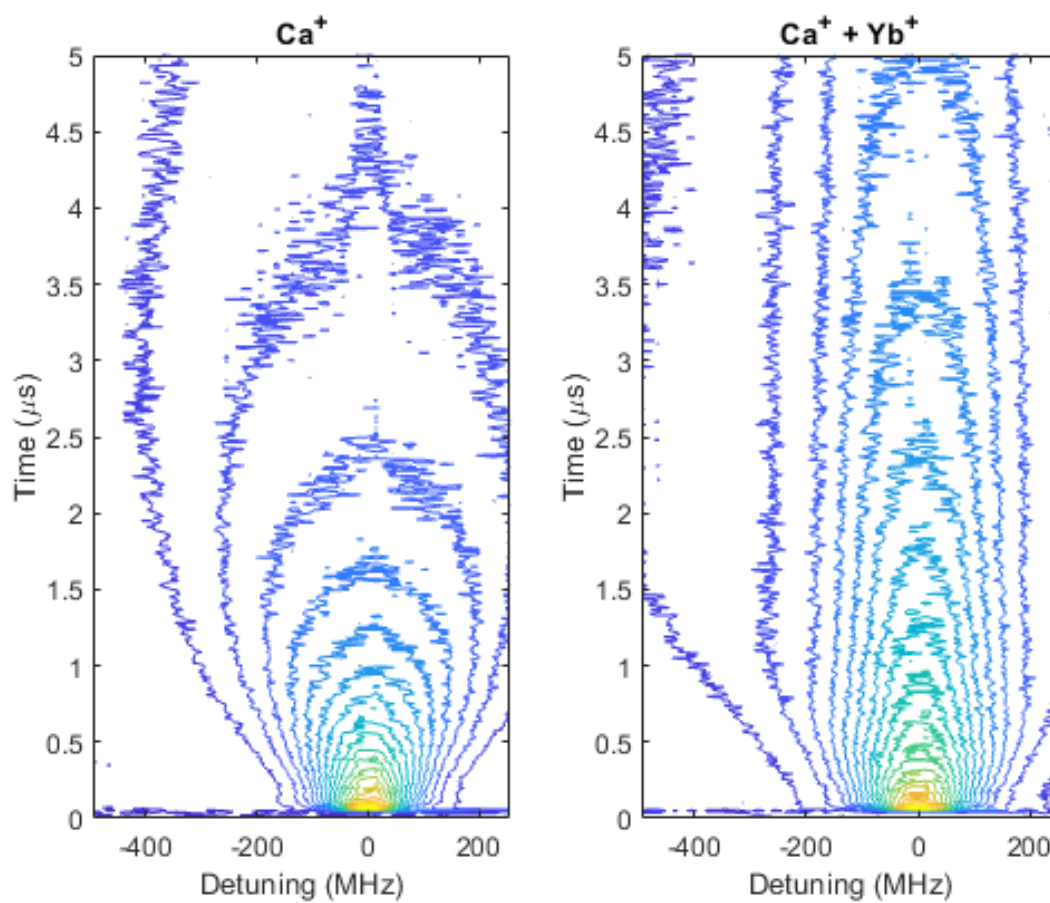
Figure 3.3 This is a contoured false-color plot. The contours show the equal signal lines of the false-color plot. The plot on the left shows the evolution of Ca^+ while the plot on the right shows Ca^+ evolution in the presence of Yb^+. Comparing the two together, it is evident that the presence of Yb^+ slows down the expansion of Ca^+.
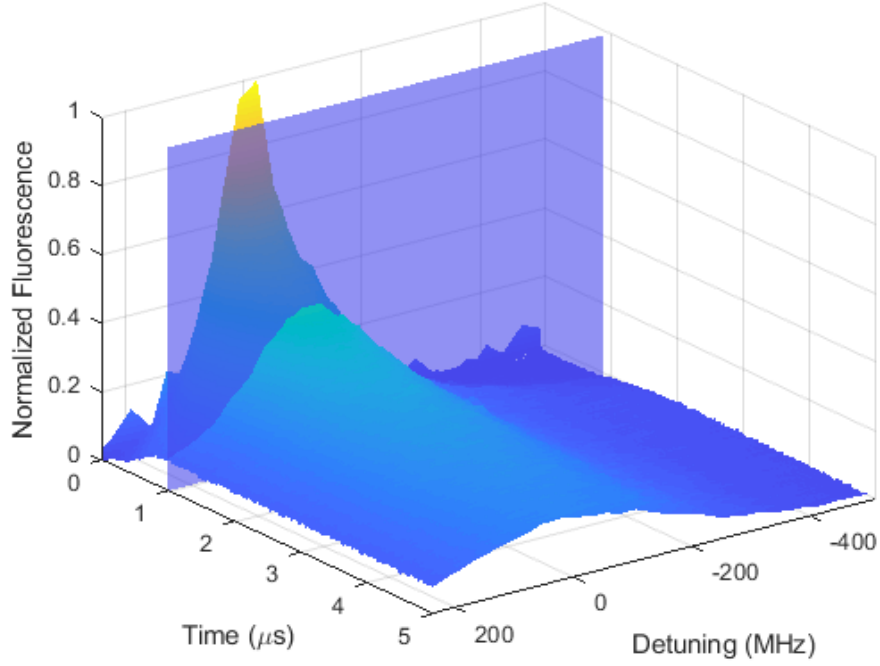
Figure 3.4 This is the same plot in Fig. 3.2 but in 3D, with the signal strength in the *z* direction. The semi-transparent plane in the figure is used to visualize a slice of data used for fitting a Voigt profile.

is determined by extracting the fluorescence vs. detuning at a particular time from the false-color plot, as shown in Fig. 3.4. We fit a Voigt profile to the experimental data, as shown in Fig. 3.5.

A Voigt profile is a convolution of a Gaussian profile, from the Doppler broadening, and a Lorentzian profile, from the atomic line shape, given by

$$V(v) = \int L(v - v')G(v')dv'. \tag{3.1}$$

In this equation L and G are the Lorentzian and Gaussian profiles, expressed as

$$L(v) = \frac{\gamma/\pi}{v^2 + \gamma^2} \tag{3.2}$$

and

$$G(v) = \frac{1}{\sqrt{2\pi}v_{rms}} \exp(v^2/2v_{rms}^2), \tag{3.3}$$

Figure 3.5 The comparison of the experimental data against a fitted Voigt profile.
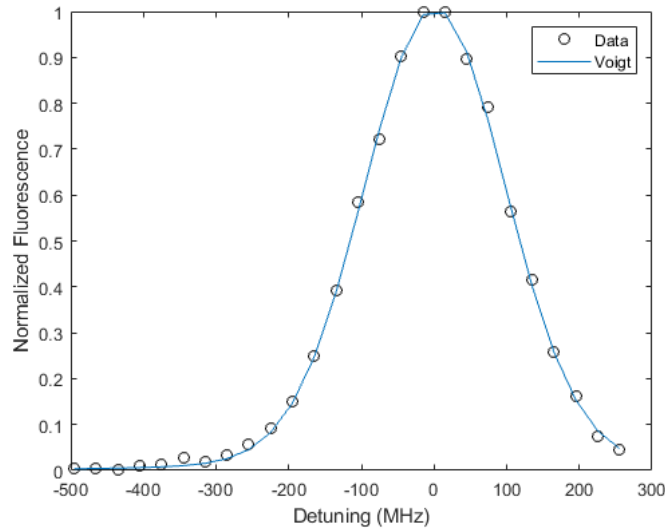
where ν is the frequency detuning from resonance and γ is the half width half max (HWHM) of the atomic transition. The root mean square (rms) Gaussian width is ν_{rms}, and is used as a fitting parameter to the Gaussian distribution.

The data is averaged in 10 ns increments and fit using the Voigt profile up to 5 μs in time. This allows us to plot out the ν_{rms} as a function of time for the first 5 μs of expansion for Ca^+ and Ca^+ + Yb^+ plasmas, as shown in Fig. 3.6. From the expansion plot, comparing the Ca^+ and the Ca^+ + Yb^+, it is clear to see that Yb^+ is coupled with Ca^+. The fact that Ca^+ in the presence of Yb^+ has a slower expansion suggests that Yb^+ exerts a friction force on the Ca^+ ions in the plasma expansion. A comparison of the exact solution to the Vlasov equation to experiment can be seen in Fig. 2.14.

The Vlasov equation is limited in that it assumes collisionless expansion. Knowing this we can see that in the single species case collisions can safely be neglected. In the dual species case if we neglect collisions then we would expect Ca^+ and Yb^+ to expand under the influence of the ambipolar field alone. Illustrated in Fig. 2.14, it is clear that this is not the case and that ion collisions cannot be neglected. This is because the Ca^+ ions are collisionally coupled to the heavy
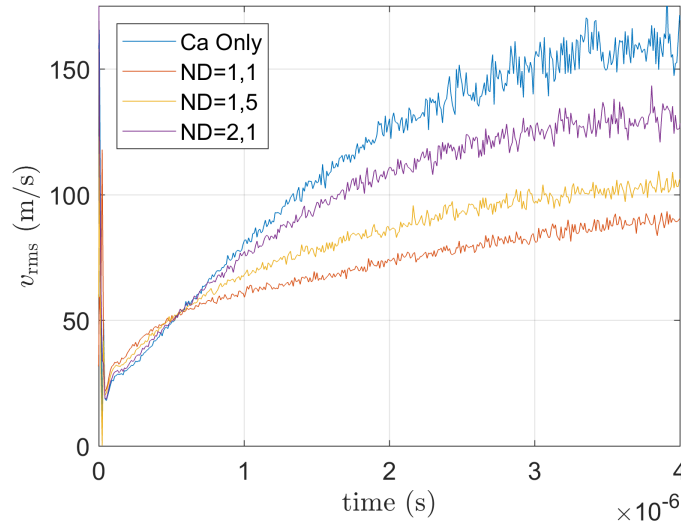
Figure 3.6 A comparison for various density ratios for Ca^+ plasma expansion. The blue curve is the expansion of Ca^+ with no Yb^+ present. The other 3 curves show the influence of different Yb^+ densities where the red curve is Yb^+/Ca^+=1. ND stands for neutral density, larger numbers correspond to larger attenuation. The ND filters attenuate the ionizing laser beams for Yb^+.

Yb^+ ions in the plasma. The Vlasov equation must be solved with a friction term added. It is no longer analytically solvable in this case and so a numerical PIC method is adopted.

3.3   Dual species plasma model

A PIC numerical model is used to determine the relevant physics in both the single and dual species plasmas. The single species plasma PIC model is compared to experimental data to verify the code. Ion friction is then added to the code and compared with the dual species plasma experimental line shape. The model was developed by Dr. Ross Spencer at Brigham Young University.

3.3.1 Single species case

In the collisionless regime, Ca^+ expansion is driven by the ambipolar field, Eq. 2.15. The PIC code assumes an initial Gaussian density profile and evolves Ca^+ ions according to Newton's second law under the influence of the ambipolar field. The initial ion temperature is set to zero, $T_i = 0$, and the disorder induced heating, Eq. 2.25, is added in quadrature at the end of the calculation. In our experiments we are only able to probe the projected velocity in the z direction. The PIC code tracks the density, acceleration, position and radial velocity of the ions. In order to compare the PIC code with experiment, we project the radial velocity of the ions in the z direction. Plotting the rms velocity as a function of time, the PIC method realizes the experimental data for a Ca^+ single species plasma, as shown in Fig. 2.14.

3.3.2 Dual species case

We have already seen that the single species collisionless treatment does not work in the dual species plasma case because of the collisional coupling between the two plasmas. For this reason a friction force is added to the PIC code to account for ion-ion collisions, Eq. 2.24. Also the density is adjusted to include both Ca^+ and Yb^+ ion density profiles,

$$n_t = n_{Ca} \exp\left[\frac{-r^2}{2\sigma_{Ca}^2}\right] + n_{Yb} \exp\left[\frac{-r^2}{2\sigma_{Yb}^2}\right], \tag{3.4}$$

where n_α is the Ca^+ and Yb^+ ion densities, σ_α is the Ca^+ and Yb^+ absorption cross section and r is simply the radial coordinate. The Ca^+ ions are evolved just as the single species expansion case with the ambipolar field given in Eq. 2.23 as well as the friction force caused by the hydrodynamic flow of the Yb^+ ions, Eq. 2.24. The additional force will "steal" kinetic energy from the Ca^+ ions and impart that energy into the hydrodynamic flow of the Yb^+ ions. Future work in measuring Yb^+ expansion with and without Ca^+ present would complete the dual species expansion picture and verify this claim. Comparisons between Yb^+, Ca^+ and $Ca^+ + Yb^+$ shows that the Ca^+ expansion
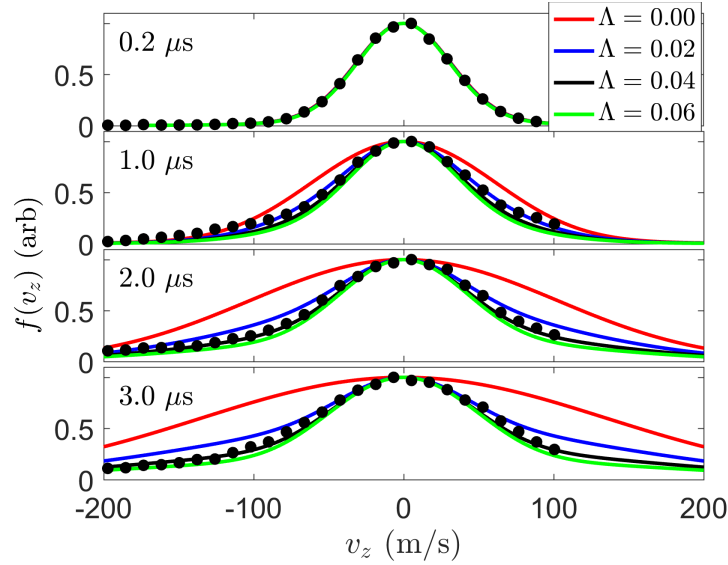
Figure 3.7 Similar to Fig. 3.5, this figure shows the velocity line shape at 0.2, 1.0, 2.0 and 3.0 μs vs numerical PIC results for various values of the Coulomb logarithm (red, blue, black and green curves). From this plot we determine the Coulomb logarithm to be 0.04.

in the presence of Yb$^+$ expands more slowly. Likewise, we would expect Yb$^+$ expansion in the presence of Ca$^+$ to expand more rapidly.

The dual species friction term, Eq. 2.24 includes the Coulomb logarithm, Λ. In the PIC code we assume Λ is a constant that does not vary in time. We then compare the PIC method with experimental data by comparing the line-shapes at $t = 0.2, 1, 2$ and 3 μs for various values of the Coulomb logarithm, Λ, as shown in Fig. 3.7. We can see that the best value for the Coulomb logarithm in this strongly-coupled plasma is $\Lambda = 0.04$.

3.4 Coulomb logarithm (Λ)

The Coulomb logarithm in the strongly coupled regime does not follow the Landau-Spitzer model, Eq. 3.9. Various attempts have been made by plasma theorists to extend the Coulomb logarithm into the strongly coupled regime, [34, 45]. None of these have been experimentally verified. We

compare the best value of the Coulomb logarithm given by experimentally verified PIC calculations to a theoretical extension into the strongly coupled regime.

Theoretical work done by L. G. Stanton and M. S. Murrillo gives the Coulomb logarithm in the strongly coupled regime as [34],

$$\Lambda = \frac{1}{2}\ln\left[1 + \left(\frac{\lambda}{\tilde{r}}\right)^2\right]. \tag{3.5}$$

In this equation λ is the total screening length and $\tilde{r}$ is the distance of closest approach with an electron screening correction,

$$\tilde{r} = r_0 W\left(r_0/\lambda_D\right). \tag{3.6}$$

Where r_0 is the classical distance of closest approach as interpreted in the Rutherford model, λ_D is the Debye length and $W(x)$ is the Lambert-W function. If we include ion and electron screening then the total screening length is,

$$\lambda = \left(\frac{1}{\lambda_D^2} + \frac{1}{\lambda_{ion}^2}\right)^{-1/2}, \tag{3.7}$$

where λ_{ion} is the screening length due to the ions. The ion screening length is given as,

$$\lambda_{ion} = \left(\frac{\varepsilon_0 k_B T_i}{n_i e^2}\right)^{-1/2}. \tag{3.8}$$

Using the inverse scaled screening length, κ, found in Eq. 1.4, we can write Eq. 3.5 in terms of κ and the strong coupling perameter, Γ,

$$\Lambda = \frac{1}{2}\ln\left[1 + \frac{\kappa^2}{(\kappa^2 + 3\Gamma)W^2(\kappa\Gamma)}\right]. \tag{3.9}$$

In our PIC model we assume that the Coulomb logarithm does not change in time. This is not entirely true, both Γ and κ evolve as the plasma evolves [42, 43]. When recombination is insignificant, the electron and ion temperatures fall adiabatically as the plasma expands. Using the analysis in Fig. 6 of Ref. [42], the strong coupling parameter is $\Gamma = 2.1 \pm 0.2$ during the early

stages of the plasma evolution. The inverse scaled screening length, κ, however evolves in time according to the characteristic expansion time for the plasma, τ,

$$\kappa = \kappa_0 \left(1 + \frac{t^2}{\tau^2} \right)^{1/4}.$$ (3.10)

In our experiment the initial inverse scaled screening length $\kappa_0 = 0.51$. After 3 μs κ changes by 8%. Since the change is small, we assume κ is constant and take the 8% change as an uncertainty in κ. Plugging in $\kappa = 0.51 \pm 0.04$ and $\Gamma = 2.1 \pm 0.2$ into Eq. 3.9 gives,

$$\Lambda = 0.05 \pm 0.01.$$ (3.11)

Comparing the theoretical value for the Coulomb logarithm with the experimental we see reasonable agreement,

$$\Lambda_{theory} = 0.05 \pm 0.01 \quad \Leftrightarrow \quad \Lambda_{exp} = 0.04.$$ (3.12)

Chapter 4

Conclusion

The strongly coupled regime is rich with unsolved problems that are becoming more and more experimentally accessible. In this work we have experimentally created the first dual species ultracold neutral plasma. We present measurements of the Ca^+ ion velocity distribution in a Ca^+ + Yb^+ strongly-coupled plasma. We show that the dual species evolution cannot be solved using the collisionless Vlasov equation. We develop a PIC calculation that models dual species plasma evolution. Comparing the PIC calculation with the experimental Ca^+ ion velocity distribution we determine the Coulomb logarithm to be 0.04.

The current work opens up a wide range of possibilities for future experiments. In this work we measured the evolution of Ca^+ in a Ca^+ + Yb^+ dual species plasma. Our measurements indicate that kinetic energy is being taken from Ca^+ in the dual species plasma. This suggests that the energy is being imparted into Yb^+ causing a more rapid expansion. Measurements of Yb^+ evolution in the presence of Ca^+ would complete the evolution picture.

More measurements could also provide a more thorough test for verifying Eq. 3.9. We could make real temperature measurements of the ions to determine how the ions thermalize inside hydrodynamic flow. We could vary the time delay between Ca^+ and Yb^+ generation to study thermalization and stopping power. This will provide a better formulation of the ion friction force,

Eq. 2.24, and potentially two stream instability observations in an idealized environment.

Dual species ultracold neutral plasmas provide a unique window into exploring the strongly coupled regime. In our experiment we create a Ca and Yb plasma, which has a mass ratio Yb/Ca of 4. This provided a self similar study of fusion class plasmas. This means that the Coulomb logarithm in a Ca + Yb UNP can be used to describe fusion class plasmas. Our next step is to measure the Coulomb logarithm, $\Lambda(\kappa)$, as a function of the electron temperature.

Bibliography

[1] Plasma Science Committee and Plasma 2010 Committee. Plasma Science: Advancing Knowledge in the National Interest (Physics 2010). National Academies Press, Washington, D. C., 2007

[2] NRL Plasma Formulary. Naval Research Laboratory, Washington, DC, 2002.

[3] J. N. Glosli, F. R. Graziani, R. M. More, M. S. Murillo, F. H. Streitz, M. P. Surh, L. X. Benedict, S. Hau-Riege, A. B. Langdon, and R. A. London. Molecular dynamics simulations of temperature equilibration in dense hydrogen. Physical Review E (Statistical, Nonlinear, and Soft Matter Physics), 78(2):025401, 2008.

[4] T. C. Killian, M. J. Lim, S. Kulin, R. Dumke, S. D. Bergeson, and S. L. Rolston. Formation of Rydberg Atoms in an Expanding Ultracold Neutral Plasma. Phys. Rev. Lett., 86:37593762, April 2001.

[5] F. Robicheaux and J. D. Hanson. Simulation of the Expansion of an Ultracold Neutral Plasma. Phys. Rev. Lett., 88(5):055002, February 2002.

[6] R. S. Fletcher, X. L. Zhang, and S. L. Rolston. Using three-body recombination to extract electron temperatures of ultracold plasmas. Phys. Rev. Lett., 99(14):145001, 2007.

[7] P. Gupta, S. Laha, C. E. Simien, H. Gao, J. Castro, T. C. Killian, and T. Pohl. Electron temperature evolution in expanding ultracold neutral plasmas. Phys. Rev. Lett., 99:075005, Aug 2007.

[8] S. A. Ivanenko, E. A. Manykin, G. V. Naidis, B. B. Zelener, and B. V. Zelener. Recombination properties of rydberg nonequilibrium plasma created by dye laser. Laser Physics, 17:419423, 2007.

[9] S. D. Bergeson and F. Robicheaux. Recombination fluorescence in ultracold neutral plasmas. Phys. Rev. Lett., 101:073202, Aug 2008.

[10] A. Denning, S. D. Bergeson, and F. Robicheaux. Measurement and simulation of laser-induced fluorescence from nonequilibrium ultracold neutral plasmas. Physical Review A (Atomic, Molecular, and Optical Physics), 80(3):033415, 2009.

[11] G. Bannasch, J. Castro, P. McQuillen, T. Pohl, and T. C. Killian. Velocity relaxation in a strongly coupled plasma. Phys. Rev. Lett., 109:185008, Nov 2012.

[12] J. Castro, P. McQuillen, and T. C. Killian. Ion acoustic waves in ultracold neutral plasmas. Phys. Rev. Lett., 105:065004, Aug 2010.

[13] P. McQuillen, J. Castro, S. Bradshaw, and T. C. Killian. Emergence of kinetic behavior in streaming ultracold neutral plasmas. arxiv, 1409:7620, 2014.

[14] K. A. Twedt and S. L. Rolston. Electron evaporation from an ultracold plasma in a uniform electric field. Physics of Plasmas, 17(8):082101, 2010.

[15] K. A. Twedt and S. L. Rolston. Electronic detection of collective modes of an ultracold plasma. Phys. Rev. Lett., 108:065003, Feb 2012.

[16] Truman M. Wilson, Wei-Ting Chen, and Jacob L. Roberts. Density-dependent response of an ultracold plasma to few-cycle radio-frequency pulses. Phys. Rev. A, 87:013410, Jan 2013. B3

[17] Truman Wilson, Wei-Ting Chen, and Jacob Roberts. Influence of electron evaporative cooling on ultracold plasma expansion. Physics of Plasmas (1994-present), 20(7):2013.

[18] W.-T. Chen, Craig Witte, and Jacob Roberts. Plasma oscillation damping in an ultracold neutral plasma. Bull. Am. Phys. Soc., 59, June 2014.

[19] G. Bannasch, T. C. Killian, and T. Pohl. Strongly coupled plasmas via rydberg blockade of cold atoms. Phys. Rev. Lett., 110:253003, Jun 2013.

[20] Wenhui Li, Paul J. Tanner, and T. F. Gallagher. Dipole-dipole excitation and ionization in an ultracold gas of rydberg atoms. Phys. Rev. Lett., 94:173001, May 2005.

[21] P. McQuillen, X. Zhang, T. Strickler, F. B. Dunning, and T. C. Killian. Imaging the evolution of an ultracold strontium rydberg gas. Phys. Rev. A, 87:013407, Jan 2013.

[22] Paul E. Grabowski, Michael P. Surh, David F. Richards, Frank R. Graziani, and Michael S. Murillo. Molecular dynamics simulations of classical stopping power. Phys. Rev. Lett., 111:215002, Nov 2013.

[23] Renato Pakter and Yan Levin. Topology of collisionless relaxation. Phys. Rev. Lett., 110:140601, Apr 2013.

[24] K. P. Driver and B. Militzer. All-electron path integral monte carlo simulations of warm dense matter: Application to water and carbon plasmas. Phys. Rev. Lett., 108:115502, Mar 2012.

[25] Peter Hartmann, Angela Douglass, Jorge C. Reyes, Lorin S. Matthews, Truell W. Hyde, Aniko Kovacs, and Zoltan Donko. Crystallization dynamics of a single layer complex plasma. Phys. Rev. Lett., 105:115004, Sep 2010.

[26] Michael S. Murillo and M. W. C. Dharma-wardana. Temperature relaxation in hot dense hydrogen. Phys. Rev. Lett., 100:205005, May 2008.

[27] S. D. Bergeson, A. Denning, M. Lyon, and F. Robicheaux. Density and temperature scaling of disorder-induced heating in ultracold plasmas. Phys. Rev. A, 83:023409, Feb 2011.

[28] R. Maruyama, R. H. Wynar, M. V. Romalis, A. Andalkar, M. D. Swallows, C. E. Pearson, and E. N. Fortson. Investigation of sub-doppler cooling in an ytterbium magneto-optical trap. Phys. Rev. A, 68:011403, Jul 2003.

[29] Chang Yong Park and Tai Hyun Yoon. Efficient magneto-optical trapping of yb atoms with a violet laser diode. Phys. Rev. A, 68:055401, Nov 2003.

[30] Zhao Peng-Yi, Xiong Zhuan-Xian, Liang Jie, He Ling-Xiang, and Lu Bao-Long. Magnetooptical trapping of ytterbium atoms with a 398.9 nm laser. Chinese Physics Letters, 25(10):3631, 2008.

[31] S. Laha, P. Gupta, C. E. Simien, H. Gao, J. Castro, T. Pohl, and T. C. Killian. Experimental Realization of an Exact Solution to the Vlasov Equations for an Expanding Plasma. Physical Review Letters, 99(15):155001, October 2007.

[32] Senaratne, Ruwan, Shankari V. Rajagopal, Zachary A. Geiger, K. Torikoshi S. Uemura R. Yajima M. Fujiwara, Vyacheslav Ya Lebedev and David M. Weld. âĂIJEffusive atomic oven nozzle design using an aligned microcapillary array.âĂİ The Review of scientific instruments 86 2 (2015): 023105.

[33] Raab, E. L., Prentiss, M., Cable, Alex, Chu, Steven and Pritchard, D. E.. "Trapping of Neutral Sodium Atoms with Radiation Pressure." Phys. Rev. Lett. 59 , no. 23 (1987): 2631–2634.

[34] L. G. Stanton and M. S. Murillo, Phys. Rev. E 93, 043203 (2016)

[35] M. Lyon, S. D. Bergeson, G. Hart, and M. S. Murillo."Strongly-coupled plasmas formed from laser-heated solids" Sci. Rep. 5, 15693 (2015).

[36] Killian. "Ultracold Neutral Plasmas" Science 316 705-708 (2007)

[37] Michael Ramm, Thaned Pruttivarasin, Mark Kokish, Ishan Talukdar, and Hartmut Haffner. "Precision Measurement Method for Branching Fractions of Excited $P_{1/2}$ States Applied to $^{40}Ca^{+}$". Phys. Rev. Lett. 111, 023004 (2013)

[38] Gerritsma, R Kirchmair, Gerhard Zahringer, F Benhelm, J Blatt, R Roos, Christian. (2008). Precision measurement of the branching fractions of the 4p 2P3/2 decay of Ca II. The European Physical Journal D. 50. 13-19. 10.1140/epjd/e2008-00196-9.

[39] R. W. Berends, E. H. Pinnington, B. Guo, and Q. Ji, Journal of Physics B: Atomic, Molecular and Optical Physics 26, L701 (1993).

[40] J. D. Huba, *Plasma Physics* (Naval Research Laboratory, Washington, DC, 2013) pp. 1-71

[41] M. Lyon and S. D. Bergeson, "Precision spectroscopy using a partially stabilized frequency comb," Appl. Opt. 53, 5163-5168 (2014)

[42] P.McQuillen, T. Strickler, T. Langin and T. C. Killian, Physics of Plasmaa 22, 033513 (2015)

[43] T. S. Strickler, T. K. Langin, P. McQuillen, J. Daligault, and T. C. Killian, Phys. Rev. X 6, 021021 (2016)

[44] The Nobel Prize in Physics 2005. Nobelprize.org. Nobel Media AB 2014. Web. 13 Jun 2018. <http://www.nobelprize.org/nobel_prizes/physics/laureates/2005/index.html>

[45] S. A. Khrapak, Phys. Plasmas 20, 054501 (2013).